Anisotropic Rolling and Controlled Chirality of Nanocrystalline Diamond Nanomembranes toward Biomimetic Helical Frameworks

Ziao Tian,[†] Wen Huang,[‡] Borui Xu,[†] Xiuling Li,[‡] and YongFeng Mei*,[†]

[†]Department of Materials Science, State Key Laboratory of ASIC and Systems, Fudan University, Shanghai 200433, People's Republic of China

[‡]Department of Electrical and Computer Engineering, Micro and Nanotechnology Laboratory, University of Illinois Urbana−Champaign, 208 N. Wright Street, Urbana, Illinois 61801, United States

Ⓢ *Supporting Information*

ABSTRACT: Future advances in materials will be aided by improved dimensional control in fabrication of 3D hierarchical structures. Self-rolling technology provides additional degrees of freedom in 3D design by enabling an arbitrary rolling direction with controllable curvature. Here, we demonstrate that deterministic helical structures with variable rolling directions can be formed through releasing a strained nanomembrane patterned in a "utility knife" shape. The asymmetry of the membrane shape provides anisotropic driving force generated by the disparity between the etching rates along different sides in this asymmetric shape. A transient finite element method (FEM) model of diagonal rolling is established to analyze the relationships among geometries, elastic properties, and boundary conditions. On the basis of this model, a diamond-based helical framework consisting of two or three helical segments has been fabricated to mimic the shapes of natural plants. Further experiment has been done to extend this approach to other materials and material combinations, such as $MoSe_2/Cr$, Cr/Pt, and VO_2. To demonstrate the possible application accessible by our technology to new fields, VO_2-based helical microscale actuation has been demonstrated with photocontrollable bending in a selected region, as well as morphable and recognizable helix. This study offers a new way to construct helical mesostructures that combine special properties of the advanced materials, thus possess novel features and potential applications.

KEYWORDS: Diamond, rolled-up nanotechnology, biomimics, helical actuation, morphable helices
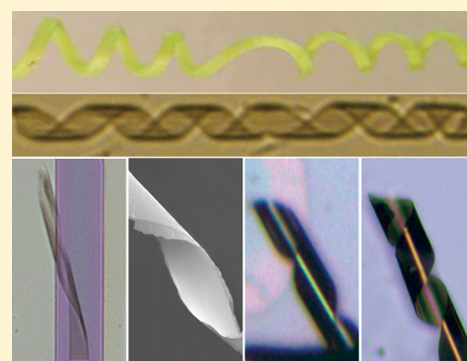
By mimicking chiral structures with broken left−right symmetry in nature, a wide range of helical micro/nanodevices based on organic and inorganic nanomembranes materials have been developed for various applications, including gas storage,[1] sensing,[2−5] micro/nanoelectromechanical systems (MEMS/NEMS),[6−8] optoelectronics,[9] and microrobotics.[10,11] Techniques for fabrication of helix materials have been developed and normally relied on anisotropic mechanical properties. For example, helical mesostructure are fabricated taking advantage of directional self-rolling of SiGe/Si bilayer as a result of anisotropic Young's modulus.[12,13] And helix based on stimuli responsive materials are precisely defined depending on anisotropy external strain which is generated by various stimuli such as light,[14] heat,[15] and stress.[16] The applicability of those methods, however, relies on vastly different properties in materials. For isotropic materials such as amorphous, polycrystalline, and nanocrystal, a helical structure is not capable of being formed because they roll along an arbitrary direction for a given configuration.[17]

Nanocrystalline diamond (NCD) nanomembrane is known as a biocompatible material for consisting of just carbon atoms, and has been constructed into mesostructures for applications in biosensing and biomedicine.[18,19] However, approaches to fabricate helix based on NCD nanomembrane at the micro- and nanoscale are limited to its extreme hardness and isotropic properties. Here, we demonstrated that a manipulated helical structure was successfully fabricated through releasing an NCD nanomembrane stripe patterned in a certain shape (like "utility knife"). The anisotropic driving force was generated by the imbalance among the etching rates along different sides in this asymmetry shape. Based on this principle, a series of helical structures with different rolling directions were fabricated by careful design in photolithography patterns on NCD nanomembrane. A mechanical model via transient finite element method (FEM) was built to elucidate the rolling behavior and to explain the helix formation by diagonal rolling. In addition, flexible and interconnected frameworks consisting of two or three helical segments were demonstrated to mimic the shapes of natural plants. Further approach has been extended to other materials and material combinations. The VO_2-based helical structure demonstrates photo-actuatable bending as another
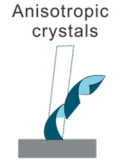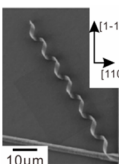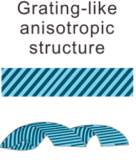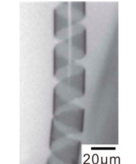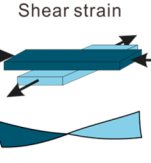
example to give biomimetic application potential accessible by this method.[20]

Considering a bilayer membrane with a strain gradient, it can spontaneously bend and twist into a helix when an anisotropic driving force is generated in the process of competition between bending and stretching. The source of driving forces and corresponding helical structures are summarized in Table 1. In an anisotropic material/strain system, Young's modulus
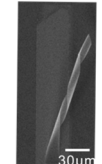
Table 1. Strategies for Fabrication of Helix

$E_x \neq E_y$		$E_x = E_y$	
Anisotropic crystals	Grating-like anisotropic structure	Shear strain	History dependence

values in the x and y directions are unequal, i.e., $E_x \neq E_y$. Hence the isotropic character originates from, e.g., crystal structure,[8,9,21,22] patterned microstructures.[23−26] The final helical structure is dependent on a misaligned angle between the anisotropic driving force direction and the stripe (or crystal) orientation. On the other hand, isotropic rubber sheet ($E_x = E_y$) forms a purely twisted shape taking advantage of an uniaxial prestretching,[27] which in the x direction is tensile strain and in the y direction is compressive strain. However, in most isotropic materials, the shearing force is too small to guide the formation of twisted or helical structure. In this work, we revealed that helical microarchitectures were fabricated through releasing a NCD nanomembrane stripe which was designed in a 2D "utility knife" pattern. The anisotropic driving force for twisting was attributed to the imbalance of the etching rates caused by designed asymmetry shape. And the anisotropic driving force led to a preferential rolling of released nanomembrane.

One significant highlight of this method is that it enables 2D patterns to be self-rolled into desired 3D structures. As etching proceeds isotropically from all sides, nanomembrane rolling along the short side was easily obtained by releasing a rectangular NCD nanomembrane as shown in Figure 1a, which could be attributed to a history-dependent process.[28] Although rolling along the short side is a common rolling behavior, but in most of the previous reports, rolling along the long side is actually energetically preferred because double-curvature at the curved edge has a lower elastic energy at those locations.[29] To realize rolling along the long side, a very narrow ribbon has been fabricated to enable quick release from the substrate. When the etching time is sufficiently short, the influence of history-dependent decrease, as well as the possibility of short-side rolling as shown in Figure 1b. Another critical influence on the shaping 3D structures is the fixed boundary condition. For example, a zag-zig ribbon with two fixed ends has been fabricated as shown in Figure 1c by dashed lines. In the bending case, the fixed boundary limits strain relaxation in the long side direction, and the strain is relaxed via
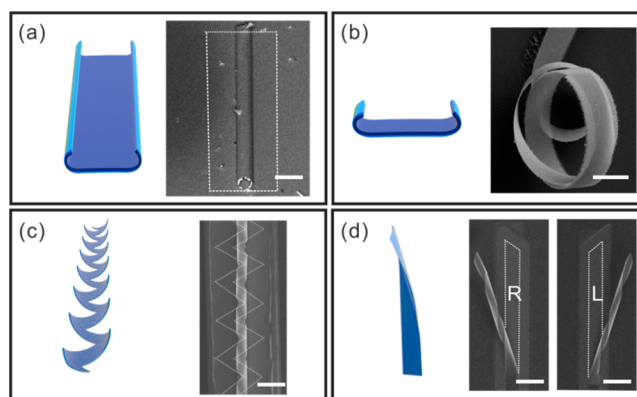
Figure 1. Geometry effect on rolling behavior according to different scenarios: (a) rolling along the short side, (b) rolling along the long side, (c) corner assisted rolling, and (d) diagonal rolling. Dashed white lines indicate original shape. Scale bars: 30 μm.

bending in the short-side direction to roll into a 3D jagged ribbon. It is especially true that the three factors mentioned above are believed to be the dominant ones in determining the final shape, and provides an extra degree of freedom in 2D pattern design. In this work, a "utility knife"−shaped NCD nanomembranes has been fabricated as shown in Figure 1d by dashed lines, which generates anisotropic mechanical stresses by the imbalance among the etching rates in this asymmetry shape. Using this deterministic rolling behavior, a helical structure has been realized. Depending on the geometry of the ribbon head, different chiral shapes are formed, such as left-handed and right-handed helices. This bending behavior is unique compared to previously report and is not capable of being predicted using previously developed models.

For understanding the underlying physical mechanisms that govern the formation of the helical structure, a model has been established to investigate rolling behaviors of "utility knife"-shaped NCD nanomembranes with various corner angle (θ) as shown in Figure 2a-I. The RIE-thinning method has been employed to regulate the geometry and the thickness of NCD nanomembranes, where a thinner film has a length of 150 μm, a width of 15 μm, and a thickness of 40 nm while a connected thicker film (blue color) acted as a bonding site as shown in Figure 2a. More details of the fabrication process are discussed in Figure S1. Afterward, the sample was immersed into HF solution for a period of time depending on the thickness of NCD nanomembranes, so as to under-etch the SiO_2 layer beneath the NCD nanomembranes pattern. As a result, thinner NCD films were released first from substrate and became free-standing while thicker NCD films adhered to substrate, which later become the bonding site supporting the final released helix. According to our previous report, NCD films can be divided into two layers: tensile strain layer close to interface between films and substrates, and relaxed layer close to the surface.[30] After relaxed from substrate, NCD nanomembranes rolled downward toward substrate because of the gradient of contraction induced by the isotropic strain relaxation in NCD layers. We assume that rolling starts at the head of "utility knife" (as shown in Figure 2a-II) due to the narrower width in the head part as compared with that in the ribbon part with the same etching rate. Such rolling keeps going when the releasing continues and thus enables the sample to form a helical structure with the rolling direction (α) as shown in Figure 2a-III. More interestingly, α can be adjusted by controlling θ.
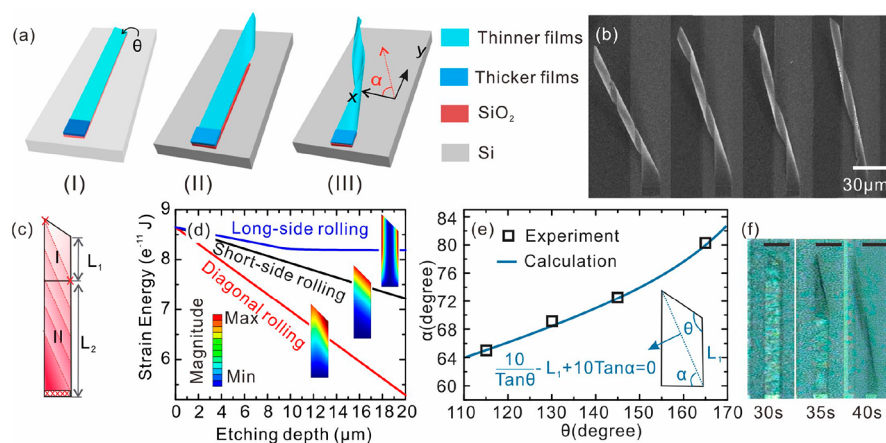
Figure 2. Evolution of rolling state of NCD nanomembranes and rolling control. (a) Schematic illustration of three stages in the rolling process. (b) SEM images of diamond helices with different θ. The samples from left to right have inclined angle θ = 115°, 130°, 145°, and 165°, respectively. (c) Schematic illustration of the diagonal rolling model setup and parameters. (d) Calculated strain energy as a function of etching depth for different rolling behavior. Insets show the displacement contour plot from FEM of the "utility knife" shapes. (e) Comparison of calculation and experiment for rolling direction α at various corner angle θ. Inset shows sketch of a diagonal rolling behavior. Blue arrow indicates rolling direction. (f) Optical images of "utility knife"-shaped NCD at three different etching times in HF solution. Etching time from left to right are 30, 35, and 40 s, respectively. Scale bar: 50 μm.

Prepatterned diamond nanomembranes are designed to have various θ, 115, 130, 145, and 165 deg. Their corresponding SEM images with various α, 65, 69.5, 72.9, and 80 deg are shown in Figure 2b from left to right, while the rolled-up helices are formed after releasing from the substrates.

To explain the diagonal rolling process and identify its governing parameters, we define two different intermediate states to simulate the entire etching process with two different etching depths L_1 and L_2 as shown in Figure 2c, where L_1 is a critical length representing the minimum length allowed the film bending which occurs only for a sufficient bending strain and L_2 is a length of the designed helical size (more details are shown in Figure S2). At the first rolling step, a right trapezoid-shaped NCD nanomembrane represented by region I is released from substrate while the other part still adheres to substrate. The rolling behavior starts at the corner with a θ angle and the rolling along the direction which is determined by the total energy minimization under certain boundary conditions. As a result, rolling direction is observed along the lines between two crosses in Figure 2c. Thus, a "dog ear" structure can be formed and keep rolling in the region II. This "dog ear" shape dominated by diagonal rolling has also been observed at the beginning state in the rolling of a rectangular bilayer based on polymer, but disappeared once the rolling continued because of a dead-lock point,[31,32] so we believe that there is no boundary condition fulfilled as in our case. At the second rolling step, the release continues in the region II gradually from substrate. The diagonal rolling will keep going toward dashed red lines and thus enables to the formation of a complete helical structure. Importantly, the rolling direction in region II is the same as one in the first step (region I). It is because any change in the direction must adapt to a larger curvature, thus costing extra associated energy. Considering elastic energy for different intermediate states, we can explain the diagonal rolling behavior by total energy minimization. The released elastic energy for rolling along long-side, short-side, and diagonal directions as a function of etching depth are calculated by assuming that the etching depth varies linearly in the equilibrium value as shown in Figure 2d. The insets magnitude in Figure 2d show the Z-displacement contour plot

of the FEM of "utility knife" shapes with various rolling directions. It is obvious that diagonal rolling (red line) presents the lowest strain energy released compared with short-side and long-side rolling. Hence, it is worthwhile to point out that boundary condition including geometry and fixed points play an important role in our directional rolling. We notice that the fixed bounding boundary condition at the fixed end of the ribbon is incompatible with the long-side rolling, which will drive upward the free end and bring about some more elastic energy.

To qualitatively illustrate control of helixes, Figure 2e shows that the experimental results of rolling direction α at a certain corner angle θ for four sets of samples as shown in Figure 2b. On the basis of the discussion above, we propose an empirical model to precisely estimate the rolling direction. The α as a function of θ and L_1 should be satisfied as

$$\frac{10}{\tan(\theta)} - L_1 + 10\tan(\alpha) = 0 \tag{1}$$

and is shown in the blue line of Figure 2e for L_1 = 23.2 μm, which can agree well with our experimental data (black squares). To simplify eq 1, we apply a linear dependence equation as α = 0.3 × θ+30.5° in the following. Hence, once θ of 2D pattern is designed, a corresponding helical structure will be formed with deterministic self-rolling direction α. A deformation history of a helix has been experimentally proved by observing a change with the nanomembranes during etching, which verifies the diagonal rolling behavior as shown in Figure 2f. At the beginning of the etching time (about 30 s), the head of the "utility knife" is released slightly but still adheres to the substrate shown in the left of Figure 2a. It is observed that the color of the films starts to change at the head first, which is due to the narrower width in the head as compared with that in the bottom with the same etching rate. After etching for 35 s, shown in the middle of Figure 2a, a right trapezoid-shaped NCD nanomembranes starts rolling from the head of the "utility knife" and bending was observed in combination with diagonal rolling while the remaining part is still adhered to substrate. Finally, diagonal rolling keeps going when the release continues.
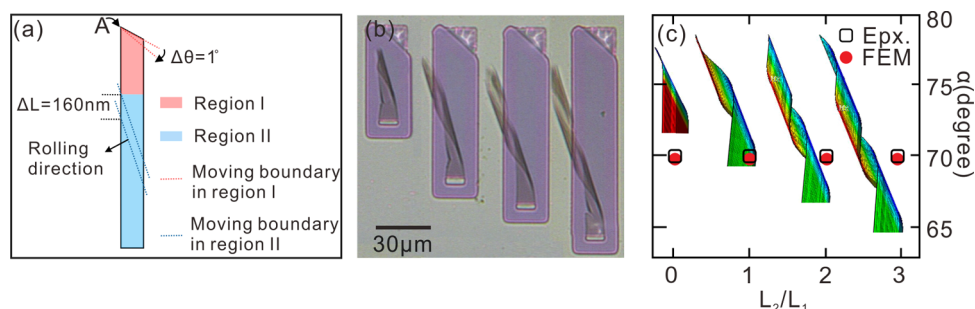
Figure 3. Quantitatively continuous control of the configuration. (a) FEM modeling methodology of NCD thin film helical rolling. (b) Optical images of diamond helices with different aspect ratio L_2/L_1. The samples from left to right have aspect ratio L_2/L_1 = 0, 1, 2, and 3, respectively. (c) Comparison of calculation and experiment for several of rolling direction α measured for four different aspect ratios. Insets are displacement contour plot from FEM of the "utility knife" shapes at various aspect ratio L_2/L_1.

Next, we use finite element method (FEM) simulation to quantitatively calculate the rolling direction by varying the length of the ribbon. A model was established to simulate the entire etching process with two intermediate states as show in Figure 3a. More details are shown in Figure S3. The state 1 rolling occurs in region I defined by the etching depth of L_1, which determines the rolling direction of NCD thin film. Beyond region I, the state 2 rolling is history dependent in region II defined by the etching depth of L_2. Moving boundary condition in FEM was programmed to model the dynamic etching progress of the SiO_2 sacrificial layer. The paths of moving boundary in both regions set up in simulation is shown in Figure 3a by dashed line. In region I, the front of moving boundary is rotating around point A with step size of $\Delta\theta = 1°$, and in region II a constant step size of $\Delta L = 160$ nm was set along the etching depth of L_2. To model the rolling mechanism of NCD thin film, two-layer shell elements with governed accuracy was used to represent the residual stress gradient of NCD thin film from bottom to the top. Isotropic and linear elastic Young's modulus of 910 GPa and Poisson coefficient of 0.2 were set to model the material properties of NCD thin film. The thermal expansion coefficients of the bottom and the top layers are set to be zero and 9.61×10^{-7} respectively with temperature increment of 5000 °C to obtain a reasonable value of residual stress of NCD thin film in experiment.[33] To showcase the feasibility with a simple example, we adjusted a series of prepatterned "utility knife" shaped diamond membranes with various aspect ratios L_2/L_1 = 0, 1, 2, and 3 to control the helical periodicity as shown from left to right in Figure 3b. We summarize the experimental data and compare it with the simulation results on helical periodicities in Figure 3 (c). When the nanomembrane has an aspect ratio of 0, according to corner effect model, the bending direction always follows the rolling direction of obtuse-angled corner. As the increase of aspect ratio from 1 to 3, interestingly, none of these samples would roll into a tube along long-side, but roll up to helices with the same rolling direction. On the basis of the observations of experiment and simulation, we can argue that the rolling behavior of "utility knife" shape must only depend on the L_1 and not on L_2. Moreover, Diagonal rolling quantitatively exhibits the continuous control of the configuration, such as the number of turns and pitch, by using different length of diamond nanomembranes ribbon.

Concatenated three-dimensional (3D) helices of opposite chirality by a perversion are ubiquitous in natural.[16,34,35] For instance, cucumber tendril coils allow the plant to wend its way to sunlight. One interesting issue is that a small straight

segment, called a perversion, is observed connecting two helices that have opposite handedness (see top of Figure 4a). The
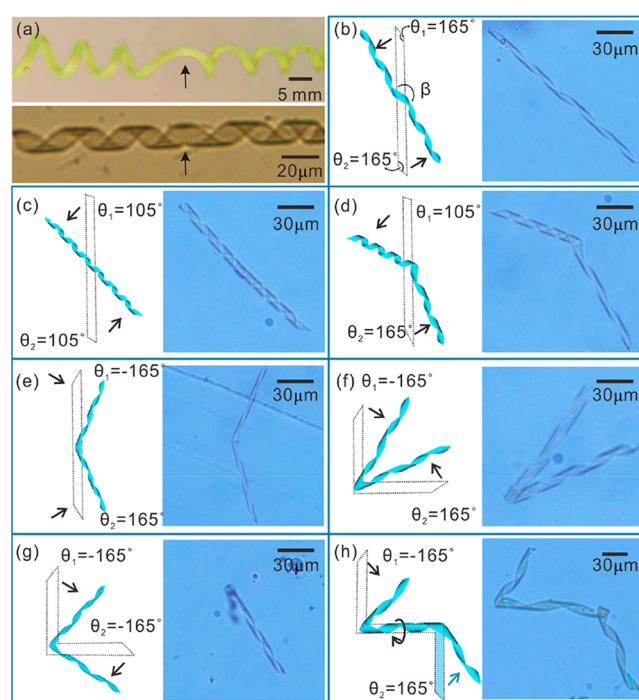
Figure 4. Interconnected frameworks by concatenation of two or more helices. (a) Tendrils of cucumber with a perversion separating two helices of opposite chirality (top) and biomimetic diamond helices (down). The black arrow indicates a perversion. Cylindrical helices formed along a straight "utility knife" shaped ribbon with (b) $\theta_1 = \theta_2 = 165°$, (c) $\theta_1 = \theta_2 = 105°$, (d) $\theta_1 = 105°$, $\theta_2 = 165°$, and (e) $\theta_1 = -165°$, $\theta_2 = 165°$. For two successive frameworks formed by a 90° turn in the planar ribbon at the junction with (f) $\theta_1 = -165°$, $\theta_2 = 165°$ and (g) $\theta_1 = \theta_2 = -165°$. (h) "S" shape with three helices.

perversions make longer circular movements in the air in search of a point that can be used for supporting.[35] We fabricated interconnected frameworks by concatenation of two helices to mimic the morphology of cucumber tendril coils (bottom of Figure 4a). First, the concatenated helices formed along a straight "utility knife" shaped ribbon have been fabricated. For the concatenation with the same chirality, as shown in Figure 4, parts b−d, the angle β formed at concatenated junction can be empirically expressed as

$$\beta = \pi - |\alpha_1 - \alpha_2| = \pi - 0.3 \times |\theta_1 - \theta_2| \quad (2)$$

where α_1 and α_2 are rolling direction of adjacent helices, each of which have a connect with θ (more details are shown in Figure S4). For example, the sample with $\theta_1 = \theta_2$ (Figure 4, parts b and c), yield $\beta = 180°$. It is easily understood that the rotation of 2D ribbon (dashed line in Figure 4) is always along the helix axis, thus a straight rotation center line caused by the same rolling direction α in both segments yields a straight tube. It is also worthwhile to note that smaller θ can lead to a more progressive shortening of the helix pitch. In practice, arbitrary variation in both angles are possible. For example, the sample with $\theta_1 = 105°$ and $\theta_2 = 165°$ yield $\beta = 162°$ (Figure 4d). On the other hand, for the concatenation with a different chirality as shown in Figure 4e, the angle β is expressed as a sum of α

$$\beta = |\alpha_1| + |\alpha_2| = 61° + 0.3 \times (|\theta_1| + |\theta_2|) \qquad (3)$$

For example, the sample with $\theta_1 = -165°$, $\theta_2 = 165°$ give $\beta = 160°$. Note that, in the case of straight pattern, β is restricted to the small range of $100° < \beta < 180°$. To tune β in wide-angle range, we introduced a turn by 90° in the planar ribbon at the junction as shown in Figure 4, parts f and g. There are two kinds of structures associated with rolling behavior. One of which deforms into a 90° turn in the helix state since the two 90° turn ribbons roll up in the same direction, while the other one rolls up a tight "V" shape with $\beta = 50°$ since the rolling direction is opposite. β can be calculated by the following equation

$$\beta = \frac{\pi}{2} - |\alpha_1 - \alpha_2| = \frac{\pi}{2} - 0.3 \times |\theta_1 - \theta_2| \qquad (4)$$

Thus, by careful design of θ, a wide angle range of $38° < \beta < 180°$ at the junction has been achieved. Using these design rules, it is straightforward to predict the shapes of more helical segments. For example, the design of an "S" shape with equal lengths ribbon but different thickness (blue ribbon with thickness of 40 nm, two 90° turn ribbons with thickness of 60 nm), roll into the multihelical structure with three helical segments as shown in Figure 4h. Together, the design rules established here suggest that it should be possible to fabricate concatenated multihelices that trace out arbitrary 3D space curves.

To demonstrate the capability of our approach, further experiments have been done to extend this approach to other materials and material combinations outlined in Figure 5a: diamond, $MoSe_2$/Cr, Cr/Pt, and VO_2. It illustrates the applicability of this method to additional classes of materials, including dielectrics, 2D transition metal dichalcogenides (TMD), metals, and phase transition materials. These materials grow in identical growth conditions but can be well applied to form helical structures. For example, nanocrystalline diamond nanomembranes were grown by the hot-filament-assisted CVD technique at 680 C° using a predominantly methane/hydrogen growth chemistry. Monolayer TMD, $MoSe_2$, were synthesized by CVD at 720 °C. Cr/Pt bilayers were grown by e-beam evaporation at room temperature. Polycrystalline VO_2 nanomembranes were grown using a radio frequency magnetron sputtering of a V_2O_5 target at 550 °C. In other words, a wide range of polycrystalline or amorphous nanomembranes can roll into 3D helices using this method employing appropriate 2D pattern. These 3D helices combine special properties of the advanced materials and thus possess novel features and potential applications.

We have selected vanadium dioxide (VO_2) as an example to give a flavor of actuation application accessible by our
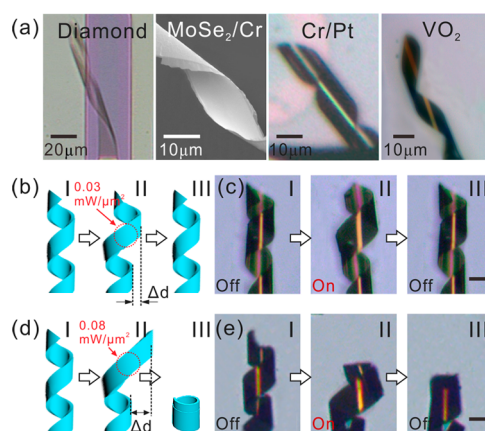
Figure 5. Helices with various advanced material compositions and novel features. (a) Optical images of rolled-up helices made of diamond, $MoSe_2$/Cr, Cr/Pt, and VO_2. (b) Schematic illustration of VO_2-based helices trigged by 808 nm laser with power density of 0.03 mW/μm^2. I to III indicate actuating behavior upon on−off laser. (c) Corresponding optical images of VO_2-based helices. (d and e) Same actuation experiment but increasing the power density to 0.08 mW/μm^2. The red circle represents laser spot. The scale bar is 30 μm.

technology. Vanadium dioxide is a strong correlated electron material with intriguing metal−insulator transition (MIT).[36] The phase transition of VO_2 will generate 1−2% compressive strain during the transition process from insulator phase to metal phase which can be applied in actuatation.[36] VO_2-based helices by rolling-path controlled mechanism are shown in Figure 5 (reversible actuation, b and c; morphable change, d and e). In the parts b and c of Figure 5, the VO_2 helical device is trigged by laser (808 nm) with power density of 0.03 mW/μm^2 which was focused with ∼30 μm in diameter on the VO_2 surface. At the beginning, the VO_2 nanomembrane rolls into helical structure due to the strain gradient inside film (schematic illustration and corresponding optical image are shown in Figure 5b-I and Figure 5c-I). After laser irradiation is positioned in the middle of helix (the red circle shown in Figure 5b-II), the phase transition happens due to laser-induced heating, leading to additional compressive strain. Therefore, the diameter of helix is increased with Δd where the laser beam is positioned (Figure 5b-II and Figure 5c-II). After turning off the laser, VO_2 suffers from an opposite transition and the rolling is influenced by that history of constrained rolling. As a result, the helix rolls back to the original helical structure again (Figure 5b-III and Figure 5c-III). All above-mentioned processes are shown in Supporting Movie 1. Since our proposed rolling is history-dependent, the above actuation could be adopted to prove our rolling principle and mimic such unique behavior. As laser excitation power density is increased to 0.08 mW/μm^2, Δd is larger than that driven by 0.03 mW/μm^2 as shown in Figure 5, parts d and e. This difference is due to the fact that more energy from light is converted to heat leading to a big phase transition area. Simulation on the surface temperature distribution of VO_2 actuator for different laser illumination is shown in Figure S5 and verifies the light−heat conversion mechanism. Interestingly, after turning off the laser, unfolded VO_2 nanomembrane rolls into a tube from short side but not a helix (as shown in Figure 5d-III and Figure 5e-III). This is because that the end of constrains and fixed boundary effects are removed and thus the rolling process is history-independent. Such morphable behavior is shown in Supporting

[Movie 2](#). The above experiments display light-actuatable bending in a selected region, as well as morphable and recognizable objects. Moreover, it illustrates a newly designed for morphable 3D mesostructures which has great potential in the fields of artificial muscle, biomimics and robotics.

In conclusion, we have demonstrated the fabrication of microscale NCD helices by patterning the thin film into the "utility knife" shape. The helical microscale architectures are formed through directional rolling by generating anisotropic mechanical stresses. On the basis of this behavior, a series of helical structures with different rolling directions have been fabricated. An empirical model has been built to provide insight into the rolling behavior and to explain the rolling direction. In addition, diamond-based helical frameworks containing two or three helical segments have been fabricated with opposite chiralities which mimic the shape of cucumber tendril coils. To demonstrate the capability of our approach, further experiments have been done to extend this approach to other materials and material combinations, such as diamond, $MoSe_2/Cr$, Cr/Pt, and VO_2. The VO_2-based helical structures serves as another example to display light-actuatable bending in a selected region, as well as morphable and recognizable objects. This study offers a simple route to design self-rolled helical mesostructures for potential applications including artificial muscle, biomimics and robotics.

ASSOCIATED CONTENT

Ⓢ Supporting Information

The Supporting Information is available free of charge on the [ACS Publications website](#) at DOI: [10.1021/acs.nanolett.8b00828](#).

> (1) Fabrication process, (2) $L1$ fitting with formula, (3) transient quasi-static FEM modeling of the rolling process of NCD membranes, (4) geometrical relationship between the angle β formed at a concatenated junction and rolling direction α, and (5) photoheat conversion ([PDF](#))
>
> Movie 1 showing actuating behavior of VO_2-based helix as shown in [Figure 5](#)c ([AVI](#))
>
> Movie 2 showing morphable VO_2-based helix as shown in [Figure 5](#)e ([AVI](#))

AUTHOR INFORMATION

Corresponding Author

*(Y.F.M.) E-mail: yfm@fudan.edu.cn.

ORCID Ⓞ

YongFeng Mei: [0000-0002-3314-6108](#)

Author Contributions

Y.F.M. conceived the concept. Z.T. and B.X. carried out the fabrications and characterizations of the diamond nanomembranes and 3D structures; W.H. under the supervision of X.L. performed the theoretical modeling and numerical simulations. Z.T. WH. and Y.F.M. cowrote the manuscript. All authors discussed the results and commented on the manuscript.

Notes

The authors declare no competing financial interest.

ACKNOWLEDGMENTS

REFERENCES

(1) Furukawa, H.; Ko, N.; Go, Y. B.; Aratani, N.; Choi, S. B.; Choi, E.; Yazaydin, A. Ö.; Snurr, R. Q.; O'Keeffe, M.; Kim, J.; Yaghi, O. M. *Science* **2010**, *329*, 424.

(2) Jiang, H. L.; Xu, Q. *Chem. Commun.* **2011**, *47*, 3351.

(3) Qiu, Y.; Deng, H.; Mou, J.; Yang, S.; Zeller, M.; Batten, S. R.; Wu, H.; Li, J. *Chem. Commun.* **2009**, *36*, 5415.

(4) Jiang, H. L.; Tatsu, Y.; Lu, Z. H.; Xu, Q. *J. Am. Chem. Soc.* **2010**, *132*, 5586.

(5) Yoon, M.; Srirambalaji, R.; Kim, K. *Chem. Rev.* **2012**, *112*, 1196.

(6) Farahani, R. D.; Dalir, H.; Le Borgne, V.; Gautier, L. A.; El Khakani, M. A.; Lévesque, M.; Therriault, D. *Nanotechnology* **2012**, *23*, 085502.

(7) Prinz, V. Y.; Naumova, E. V.; Golod, S. V.; Seleznev, V. A.; Bocharov, A. A.; Kubarev, V. V. *Sci. Rep.* **2017**, *7*, 43334.

(8) Dai, L.; Zhang, L. *Nanoscale* **2013**, *5*, 971.

(9) Hwang, G.; Dockendorf, C.; Bell, D.; Dong, L.; Hashimoto, H.; Poulikakos, D.; Nelson, B. *Int. J. Optomechatronics* **2008**, *2*, 88.

(10) Abbott, J. J.; Peyer, K. E.; Lagomarsino, M. C.; Zhang, L.; Dong, L.; Kaliakatsos, I. K.; Nelson, B. J. *Int. J. Robot. Res.* **2009**, *28*, 1434.

(11) Tottori, S.; Zhang, L.; Peyer, K. E.; Nelson, B. J. *Nano Lett.* **2013**, *13*, 4263.

(12) Zhang, L.; Deckhardt, E.; Weber, A.; Schönenberger, C.; Grützmacher, D. *Nanotechnology* **2005**, *16*, 655.

(13) Hwang, G.; Hashimoto, H.; Bell, D. J.; Dong, L.; Nelson, B. J.; Schön, S. *Nano Lett.* **2009**, *9*, 554.

(14) Iamsaard, S.; Aßhoff, S. J.; Matt, B.; Kudernac, T.; Cornelissen, J. J. L. M.; Fletcher, S. P.; Katsonis, N. *Nat. Chem.* **2014**, *6*, 229.

(15) Hornat, C. C.; Yang, Y.; Urban, M. W. *Adv. Mater.* **2017**, *29*, 1603334.

(16) Gerbode, S. J.; Puzey, J. R.; McCormick, A. G.; Mahadevan, L. *Science* **2012**, *337*, 1087.

(17) Timoshenko, S. *J. Opt. Soc. Am.* **1925**, *11*, 233.

(18) Yang, W.; Auciello, O.; Butler, J. E.; Cai, W.; Carlisle, J. A.; Gerbi, J. E.; Gruen, D. M.; Knickerbocker, T.; Lasseter, T. L.; Russell, J. J.; Smith, L. M.; Hamers, R. J. *Nat. Mater.* **2002**, *1*, 253.

(19) Härtl, A.; Schmich, E.; Garrido, J. A.; Hernando, J.; Catharino, S. C.; Walter, S.; Feulner, P.; Kromka, A.; Steinmuller, D.; Stutzmann, M. *Nat. Mater.* **2004**, *3*, 736.

(20) Amaral, M.; Gomes, P. S.; Lopes, M. A.; Santos, J. D.; Silva, R. F.; Fernandes, M. H. *Acta Biomater.* **2009**, *5*, 755.

(21) Mei, Y.; Huang, G.; Solovev, A. A.; Ureña, E. B.; Mönch, I.; Ding, F.; Reindl, T.; Fu, R. K. Y.; Chu, P. K.; Schmidt, O. G. *Adv. Mater.* **2008**, *20*, 4085.

(22) Chen, Z. *Nanoscale* **2014**, *6*, 9443.

(23) Li, W.; Huang, G.; Wang, J.; Yu, Y.; Wu, X.; Cui, X.; Mei, Y. *Lab Chip* **2012**, *12*, 2322.

(24) Erb, R. M.; Sander, J. S.; Grisch, R.; Studart, A. R. *Nat. Commun.* **2013**, *4*, 1712.

(25) Jeon, S.; Hauser, A. W.; Hayward, R. C. *Acc. Chem. Res.* **2017**, *50*, 161.

(26) Zhang, H.; Mourran, A.; Möller, M. *Nano Lett.* **2017**, *17*, 2010.

(27) Yu, X.; Zhang, L.; Hu, N.; Grover, H.; Huang, S.; Wang, D.; Chen, Z. *Appl. Phys. Lett.* **2017**, *110*, 091901.

(28) Chun, I. S.; Challa, A.; Derickson, B.; Hsia, K. J.; Li, X. *Nano Lett.* **2010**, *10*, 3927.

(29) Alben, S.; Balakrisnan, B.; Smela, E. *Nano Lett.* **2011**, *11*, 2280.

(30) Tian, Z.; Zhang, L.; Fang, Y.; Xu, B.; Tang, S.; Hu, N.; An, Z.; Chen, Z.; Mei, Y. *Adv. Mater.* **2017**, *29*, 1604572.

(31) Stoychev, G.; Zakharchenko, S.; Turcaud, S.; Dunlop, J. W. C.; Ionov, L. *ACS Nano* **2012**, *6*, 3925.

(32) Aoki, K.; Ishiguro, K.; Denokami, M.; Tanahashi, Y.; Furusawa, K.; Sekine, N.; Adschiri, T.; Fujii, M. *Small* **2017**, *13*, 1701630.

(33) Huang, W.; Koric, S.; Yu, X.; Hsia, K. J.; Li, X. *Nano Lett.* **2014**, *14*, 6293.

(34) Iamsaard, S.; Villemin, E.; Lancia, F.; Aβhoff, S.; Fletcher, S. P.; Katsonis, N. *Nat. Protoc.* **2016**, *11*, 1788.

(35) Armon, S.; Efrati, E.; Kupferman, R.; Sharon, E. *Science* **2011**, *333*, 1726.

(36) Tian, Z.; Xu, B.; Hsu, B.; Stan, L.; Yang, Z.; Mei, Y. *Nano Lett.* **2018**, *18*, 3017.